PROCEEDINGS OF THE ROYAL SOCIETY A

rspa.royalsocietypublishing.org

Research

Cite this article: Zhao Z, Liu C, Ma D. 2014 Pure rotation of a prism on a ramp. *Proc. R. Soc. A* **470**: 20140007.
http://dx.doi.org/10.1098/rspa.2014.0007

Received: 4 January 2014
Accepted: 3 June 2014

Subject Areas:
mechanical engineering, mechanics

Keywords:
line impact, friction, modelling, experiments

Author for correspondence:
Caishan Liu
e-mail: liucs@pku.edu.cn

Electronic supplementary material is available at http://dx.doi.org/10.1098/rspa.2014.0007 or via http://rspa.royalsocietypublishing.org.

Royal Society Publishing

Pure rotation of a prism on a ramp

Zhen Zhao[1], Caishan Liu[2] and Daolin Ma[2]

[1]School of Aeronautic Science and Engineering, Beihang University, Beijing 100191, People's Republic of China
[2]State Key Laboratory for Turbulence and Complex Systems, College of Engineering, Peking University, Beijing 100871, People's Republic of China

In this work, we study a prism with a cross section in polygon rolling on a ramp inclined at a small angle. The prism under gravity rolls purely around each individual edge, intermittently interrupted by a sequence of *face collisions* between the side face of the prism and the ramp. By limiting the prism in a planar motion, we propose a mathematical model to deal with the events of the impacts. With a pair of laser-Doppler vibrometers, experiments are also conducted to measure the motions of various prisms made of different materials and with different edge number. Not only are good agreements achieved between our numerical and experimental results, but also an intriguing physical phenomenon is discovered: the purely rolling motion is nearly independent of the prism's materials, yet it is closely related to the prism's geometry. Imagine that an ideal circular section can be approximately equivalent to a polygon with a large enough edge number N, the finding presented in this paper may help discover the physical mechanism of rolling friction.

1. Introduction

Contacts/impacts are ubiquitous in diverse systems and phenomena that span vast ranges of scales, from the nanometre contacts inherent in micromachines and nanomachines [1] to the geophysical scale characteristics of earthquakes [2]. Despite the practical and fundamental importance in many applications, challenges still exist in many aspects of modelling contacts and impacts. For instance, solutions for the impacts occurring in an interface with either line or surface shape still remain open.

Virtually impact dynamics corresponds to an non-equilibrium process that usually manifests different-size-scaled behaviours of materials to result in both dispersion and dissipation of energy [3]. As an impact happens in an extremely small time interval and activates ignorable deformation, a rigid body model, together with a certain impact law, is often used to predict the impact output [4–6]. However, the impact laws in existing literature, e.g. the coefficients of restitution given by Newton and Poisson, mainly play a role describing the energy dissipation for an impact occurring at an isolated point [7–9]. When a finite or infinite number of points are simultaneously involved in impacts, the motions of these points are often entangled together to significantly influence the dissipation and dispersion of energy. In these cases, we need to supplement other physical laws for characterizing the coupled motions [3,10].

Quantifying the coupled motions depends on understanding the temporal behaviours of materials, which essentially should follow a constitution relationship prescribed in continuum mechanics. For impacting bodies complying with reasonable rigid approximations, the constitution relationship is often described as a spring-dashpot model with a stiffness-centralized parameter to represent the material elasticity, plus a damping coefficient to quantify dissipation of energy [11–13]. Although capable of capturing the main motion features, this technique often requires parameters that have to be determined via fitting subjected to constraints imposed by practical requirements. This is usually impossible in real physics and would cause relative large discrepancies between the predicted scenarios and reality. Moreover, when numerical results are mixed with information on different scales, the characteristics inherent in systems may be confusing due to numerical errors involved in the mixture of information.

To avoid the disadvantages of spring-dashpot models, we recently developed a new approach to solving impact problems [3,14]. Under the conventional assumptions of invariable configuration and ignorable non-impulsive forces, material behaviours due to impacts are described by a *force–energy* relationship between contact forces and elastic potential energy. This relationship is deduced mathematically from a *force–deformation* relation specific to the material. The elastic potential energy at each contact point is accumulated through integrating the normal relative velocity over the corresponding normal impulse, equivalent to the work done by the normal contact force via normal elastic deformation. By an energetic coefficient to scale the energy dissipation in the work-to-energy transition, we can obtain an instantaneous distribution for the potential energies among all the contact points, and then for the normal contact forces by the force–energy relationship. Using the instantaneous distribution, we therefore can replace the time scale in impact dynamics with an independent impulse scale and describe the impact dynamics as a model with respect to a 'time-like' independent impulse. In this model, energy dissipation is scaled by the energetic coefficient with a value limited in a range $[0, 1]$, and the energy dispersion is related to the ratios of the contact stiffness among all the points. Since these quantities can be effectively estimated either by material properties or via independent experiments, this method evades the difficulties in determining the concrete values of the stiffness and damping coefficients in a spring-dashpot model. It also avoids the numerical difficulties suffered by the stiff second-order ordinary differential equations within a small time period. The validation of this method can be found in studies performed recently over different mechanical systems [3,10,14–18].

This paper aims at extending the theory on point impacts into surface impacts. Consider a polygonal prism with N edges rolling on a ramp. A face collision occurs at the instant when a side face of the rolling prism falls down the ramp. This example has been theoretically investigated first by Abeyaratne [19], then by Stronge [4] and MacDonald [20], and recently studied in experimental work [21]. All the investigations have clearly revealed that such a simple system manifests its dynamics sophisticatedly, and indicated that the physical mechanism underlying a face collision would be much distinct from the one in a point impact.

For demonstrating the discrepancy of the dynamics between point impacts and face collisions, Ruina *et al.* [22] designed a pair of wood prisms with seven equal edges. The only difference between them is that one has flat side faces, whereas the other one has side surfaces that are slightly concave. Surprisingly, the tiny difference in their side faces will result in entirely different

motions as the prisms roll on the same ramp: the prism with flat side faces starts to roll along the ramp, whereas the one with concave side faces immediately stops after the first impact. In the electronic supplementary material,[1] we demonstrate this intriguing phenomenon using the prisms kindly offered by Ruina.

Focusing attention on the planar motion of a prism purely rolling on a fixed ramp inclined with a small angle, we simplify the face collision within the prism's motion into a two-dimensional *line impact*. In order to model the material behaviour activated by an individual line impact, we specify a linear *stress–strain* relationship to the contact interface, on which a thin *elastic boundary layer* is assigned [23]. Combination of the linear *stress–strain* relationship and the geometry of the flat surface allows the normal stress on the contact interface to form a linear distribution. As the contact stress varies with an impact process, the coefficient scale in the linear distribution changes accompanying the dispersion of energy. This permits the contact interface to be separated, and eventually makes the prism roll on the ramp. Clearly modelling the line-impact dynamics needs to correctly capture the evolution of the interface stress. For achieving this purpose, we adopt the same idea as in [3,14] to deal with the line-impact dynamics. After specific treatments, a set of first-order ordinary differential equations with respect to a 'time-like' independent stress impulse is obtained.

Modelling the dissipation of energy correctly is also crucial in dealing with a line impact. Basically, energy dissipation in impacts arises from different factors, including material plasticity, impact-activating vibration and friction. For impacts with relative small velocity, the dissipation by material plasticity can be ignored. If Coulomb's friction law is introduced, friction dissipates mechanical energy only when slip exists on the contact interface [24]. The difficult issue related to the energy dissipation comes from the impact-activating vibration, which not only takes away part of the energy, but also influences the friction property on contact interfaces [25,26].

For the line impacts in the prism's motion, we adopt Coulomb's friction law to quantify the dissipation of energy by friction. By limiting the ramp in a small inclined angle, we observe from experiments that no detachment occurs during the rolling motion of prisms. We take it as a *non-detachment condition* to terminate the process of a line impact. By this condition, the energy dissipation in a line impact is scaled without resorting to the complex physical mechanism in association with the impact-agitating vibration and other small-scaled behaviours of materials.

In order to validate the model developed in this paper, we also perform experimental investigations by measuring the motions of various prisms made of different materials and with different edge number. In our experiments, a pair of laser-Doppler vibrometers is used to provide accurate measurements. Knowledge of the time history of the simultaneous velocities at two gauged points gives information to detail the prism dynamics. Good agreements are achieved between our numerical and experimental results, and an intriguing physical phenomenon is discovered: the purely rolling motion is nearly independent of the prism's materials, yet it is closely related to the prism's geometry.

This paper is organized as follows: in §2, we present descriptions for a rolling prism, followed by the equations in dynamics and kinematics. In §3, a theoretical model is developed to deal with line impacts involved in the rolling motion of the prism. Details of experimental realization are presented in §4, including introduction of the instruments and the measurement method for using laser sensors. In §5, numerical and experimental results are compared for the motion of prisms under different conditions. Conclusion and discussion follow in §6.

2. Description for a rolling prism

Suppose a prism with mass m and length l has N equal edges and N equal pieces of flat surfaces (rectangles on sides). Figure 1 depicts a prism with $N = 8$ as an example for illustration. The

[1](1) Video of a pair of almost identical polygon prisms with edge number $N = 7$ rolling on a slope. By releasing them synchronously, the prism with flat side faces starts to roll along the slope, while the one with concave side faces immediately stops after the first impact. (2) Video of a steel prism with 24 edges on a glass slope. (3) Video of two prisms with the same shape ($N = 30$): one made from steel and one made from aluminium.

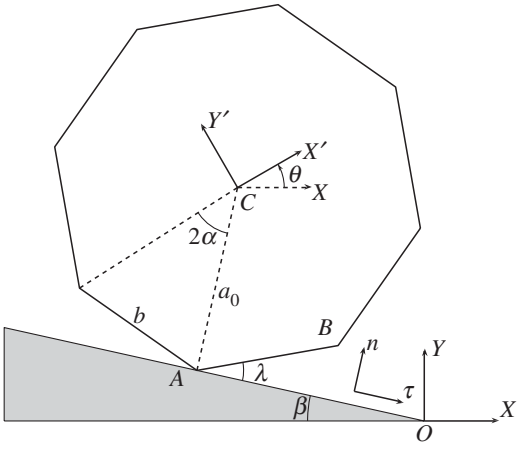

Figure 1. A prism with $N = 8$ rolling on a ramp at an inclined angle β.

distance from its centre of mass C to each individual edge is a_0, the central angle for each side is $2\alpha = 2\pi/N$ and width of the flat face is of value $b = 2a_0 \sin\alpha$. The moment of inertia about centre of mass C is $J = ma_0^2(\cos 2\alpha + 2)/6$. A ramp is inclined with a small inclined angle β. Unit vectors $\mathbf{n}$ and $\boldsymbol{\tau}$ are related to the normal and tangential directions of the ramp, respectively. Define by (O, xy) and $(C, x'y')$ an inertial frame and a body-fixed frame, respectively. The motion of a prism is fully described by x and y coordinates of mass centre C in frame (O, xy) and the rotation angle θ between frames of (O, xy) and $(C, x'y')$.

Suppose that the prism purely rotates around an edge at A and will collide against the ramp by side face AB. We denote A and B as *rolling edge* and *leading edge*, respectively. Side face AB at the current moment has an angle λ to the ramp. As the rolling edge changes after a line impact, we define $\lambda = 0$ at the start of a line impact, while $\lambda = 2\alpha$ at the end of the line impact. Parameter $\{\xi : |\xi \in D = [0, b]\}$ is used for describing the points along AB.

The motion of the prism can be classified into two modes: the *contact phase* of the prism purely rotating around an edge keeping contact on the ramp; and the *line-impact phase* when one side face falling down the ramp. During a *contact phase*, the prism is in a fixed-axis rotation whose motion can be fully described by selecting θ as the generalized coordinate. For a *contact phase*, we easily obtain the governing equation and the corresponding constraint forces at A as follows:

$$\left.\begin{aligned} J_A\ddot{\theta}(t) &= -mga_0 \sin\phi_1, \\ F_A^n(t) &= \left(\frac{6\sin\phi_1 \sin\phi_2}{\cos 2\alpha + 8} - \sin\beta\right) mg + ma_0\dot{\theta}^2 \cos\phi_2 \\ \text{and} \qquad F_A^\tau(t) &= \left(\frac{6\sin\phi_1 \cos\phi_2}{\cos 2\alpha + 8} + \cos\beta\right) mg + ma_0\dot{\theta}^2 \sin\phi_2, \end{aligned}\right\} \tag{2.1}$$

where $\phi_1 = (\alpha + \beta - \lambda)$, $\phi_2 = (\alpha + 2\beta - \lambda)$, $J_A = J + ma_0^2$, $F_A^n(t)$ and $F_A^\tau(t)$ represent the normal and tangential components of the contact force at point A, respectively.

Suppose friction satisfies Coulomb's friction law. The pure rotation can be maintained only if $F_A^n(t)$ and $F_A^\tau(t)$ satisfy conditions as follows:

$$\frac{|F_A^\tau(t)|}{|F_A^n(t)|} \le \mu_s, \quad F_A^n(t) > 0, \tag{2.2}$$

where μ_s is the static coefficient of friction. Otherwise, the prism may either slip ($|F_A^\tau(t)|/|F_A^n(t)| > \mu_s$) or detach from the ramp ($F_A^n(t) = 0$). A prism can enter into a pure rotation mode only if inclined angle β is small enough and edge number N is large.

As a side face, e.g. AB, falls down to the ramp, a *line-impact phase* is triggered. In this phase, we need three degrees of freedom to describe the prism's dynamics because the constraint equations previously applied at A for the *contact phase* are no longer established. By selecting (x, y, θ) as the generalized coordinates to describe the motion of the prism in a *line-impact phase*, the impact dynamics is governed by the following equations:

$$\left.\begin{aligned} m\ddot{x}(t) &= F_n(t)\sin\beta + F_\tau(t)\cos\beta, \\ m\ddot{y}(t) &= F_n(t)\cos\beta - F_\tau(t)\sin\beta - F_L \\ \text{and} \quad J\ddot{\theta}(t) &= M_n^c(t) + M_\tau^c(t), \end{aligned}\right\} \tag{2.3}$$

where $F_L = mg$ denotes gravity, $F_n(t)$ and $F_\tau(t)$ represent, respectively, the normal and tangential components of the resultant forces by the interaction from the ramp, $M_n^c(t)$ and $M_\tau^c(t)$ are the net moments resulting, respectively, from $F_n(t)$ and $F_\tau(t)$ about mass centre C.

Note that all the values of $F_n(t)$, $F_\tau(t)$, $M_n^c(t)$ and $M_\tau^c(t)$ are unknown now and will be determined by incorporating certain physical laws into the relative motion on the contact surface.

Components $v^n(t,\xi)$ and $v^\tau(t,\xi)$ along $\mathbf{n}$ and τ for the velocity of each point $\xi \in D$ are given by

$$\left.\begin{aligned} v^n(t,\xi) &= \dot{x}(t)\sin\beta + \dot{y}(t)\cos\beta - \dot{\theta}(t)\left(\frac{b}{2} - \xi\right) \\ \text{and} \quad v^\tau(t,\xi) &= \dot{x}(t)\cos\beta - \dot{y}(t)\sin\beta + \dot{\theta}(t)a_0\cos\alpha. \end{aligned}\right\} \tag{2.4}$$

The changing rates of $v^n(t,\xi)$ and $v^\tau(t,\xi)$ with respect to time are

$$\left.\begin{aligned} \dot{v}^n(t,\xi) &= \ddot{x}(t)\sin\beta + \ddot{y}(t)\cos\beta - \ddot{\theta}(t)\left(\frac{b}{2} - \xi\right) \\ \text{and} \quad \dot{v}^\tau(t,\xi) &= \ddot{x}(t)\cos\beta - \ddot{y}(t)\sin\beta + \ddot{\theta}(t)a_0\cos\alpha. \end{aligned}\right\} \tag{2.5}$$

If small deformation on the contact surface can be neglected, the kinematical relationships shown in equation (2.4) and (2.5) always exist. These relationships will be used later in association with the physical laws to reflect the interaction between the prism and the ramp.

3. Modelling a line impact

To solve equation (2.3) for the prism dynamics in a *line-impact phase*, other physical laws should be supplemented to determine the interaction between the side face and the ramp. For achieving this purpose, we introduce assumptions as follows:

A1. The material adjacent to the impact site behaves elastically in response of a line impact. Coupling between normal and tangential deformation is weak enough to be ignored.
A2. The small deformation of the contact surface permits the prism's configuration to be invariable and the intensity of a line impact allows the non-impulsive forces to be ignored.
A3. The line impact is limited to an intensity that cannot make the prism be in free motion as the impact vanishes.

(a) Property of the normal stress distribution

As assumption A1 is assumed, a contact interface can be modelled as an elastic boundary layer that is confined in a thin lamina between two rigid bodies of the prism and the ramp. This allows us to adopt a simple Winkler's elastic base, rather than an elastic infinite half-space, to model the material behaviours adjacent to the contact interface [23].

This model is illustrated in figure 2. The elastic layer, of small thickness $\triangle$, rests on a rigid base parallel to the ramp and is compressed by a rigid prism. Suppose no interaction between adjacent elements in tangential direction in the elastic layer. Denote by $\delta(t,\xi)$ the penetration at point $\xi \in D$. Since only compression occurs in the elastic layer, we set $\delta(t,\xi)$ just with negative

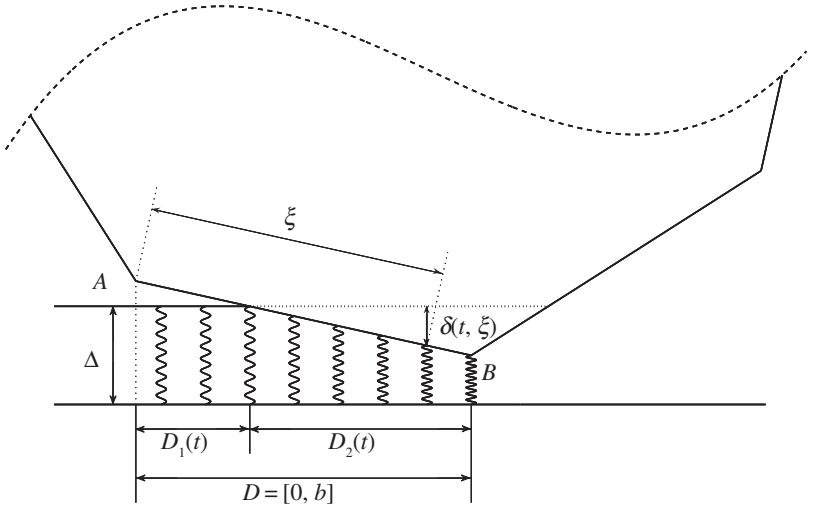

Figure 2. Elastic boundary layer on contact surface.

values and divide the contact region D into two parts: (i) the *separated region* designated by $D_1(t) = \{\xi : \delta(t,\xi) > 0\}$ and (ii) the *effective region* designated by $D_2(t) = \{\xi : \delta(t,\xi) \le 0\}$. The normal elastic strain at any point is given by

$$\varepsilon_n(t,\xi) = \begin{cases} \dfrac{\delta(t,\xi)}{\triangle}, & D_2(t) = \{\xi : |\delta(t,\xi) \le 0\} \\ 0, & D_1(t) = \{\xi : |\delta(t,\xi) > 0\}. \end{cases} \tag{3.1}$$

Within the elastic boundary layer, the normal stress $\bar{\sigma}_n(t,\xi)$ at any point on contact region D depends only on the strain $\varepsilon_n(t,\xi)$ at that point. Let us denote a linear relationship between $\bar{\sigma}_n(t,\xi)$ and $\varepsilon_n(t,\xi)$ as follows:

$$\bar{\sigma}_n(t,\xi) = E^* \varepsilon_n(t,\xi), \tag{3.2}$$

where E^* the effective elastic modulus related to the materials of contacting bodies. Noting that $\bar{\sigma}_n(t,\xi)$ and $\varepsilon_n(t,\xi)$ always take negative values along the normal of the ramp since the boundary layer is just in compression.

Denote by $\sigma_n(t,\xi)$ the interface stress applied on boundary AB of the prism. Clearly, the direction of $\sigma_n(t,\xi)$ is opposite to the one of $\bar{\sigma}_n(t,\xi)$, and we have $\sigma_n(t,\xi) = -\bar{\sigma}_n(t,\xi) \ge 0$. Unless explicitly confusion, we will always use $\sigma_n(t,\xi)$ to represent the normal interaction between the prism and the ramp.

Owing to the flat surfaces in the prism and the ramp, the interface stresses at different contact points are not independent. The limitation from the two rigid flat planes only allows elastic displacement $\delta(t,\xi)$ to vary linearly along the boundary layer. Consequently, from equation (3.2), the normal stress will be linearly distributed along the effective region of the contact boundary. The stress concentration at two corner points are not taken into account in the model.

Since $\sigma(t,\xi) = 0$ outside the effective region, figure 3 shows four possible profiles for the linear distribution of the normal stresses on the contact interface. The first two are termed DS-I and DS-II with triangle shapes, whereas the others are termed DS-III and DS-IV with trapezoid shapes.

Suppose that the stress-distribution line and contact-line AB intersect at point S. We define a variable $s(t)$ to represent the coordinate of point S in the ξ-axis. The *effective regions* in the four

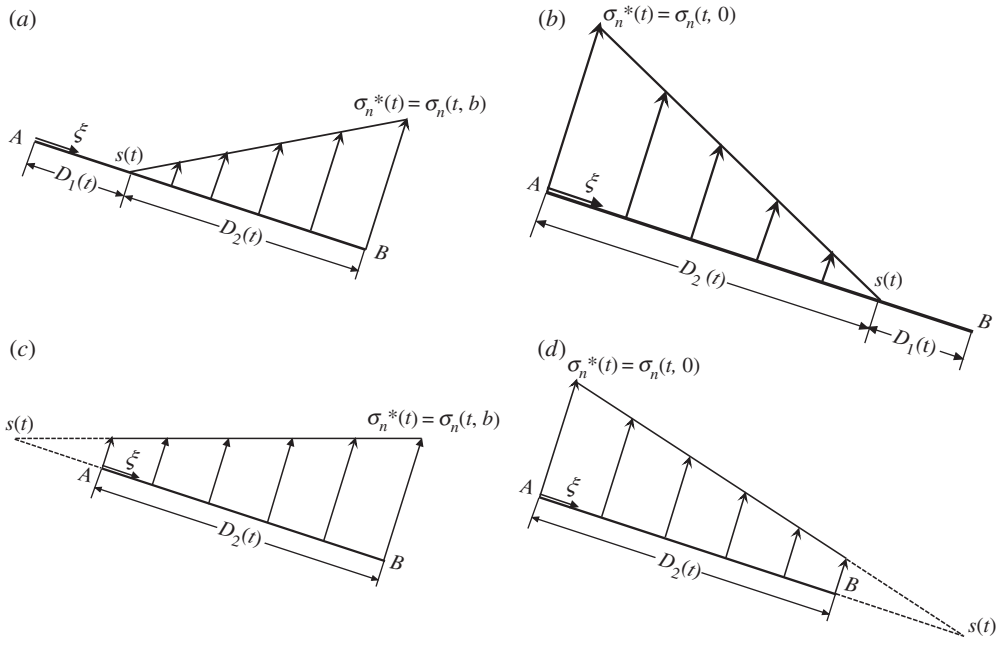

Figure 3. Instantaneous distribution of the normal stress on contact surface in (*a*,*b*) with a triangle shape, (*c*,*d*) with a trapezoidal shape. (*a*) DS-I, (*b*) DS-II, (*c*) DS-III and (*d*) DS-IV.

modes from DS-I to DS-IV can be, respectively, quantified as follows:

$$D_2(t) = \begin{cases} [s(t), b], & s(t) > 0 \text{ in DS-I} \\ [0, s(t)], & s(t) > 0 \text{ in DS-II} \\ [0, b], & s(t) < 0 \text{ in DS-III} \\ [0, b], & s(t) > 0 \text{ in DS-IV.} \end{cases} \tag{3.3}$$

For convenience of distinguishing the four modes of the normal-contact-stress distribution, we define s^* as the position of a contact point with maximum stress $\sigma_n^*(t)$. So,

$$s^* = \begin{cases} b & \text{in DS-I, DS-III} \\ 0 & \text{in DS-II, DS-IV.} \end{cases} \tag{3.4}$$

Once the mode of the normal-contact-stress distribution is given, it is clear that the normal stress at any point in $D_2(t)$ can be uniquely determined by $\sigma_n^*(t)$ and $s(t)$

$$\frac{\sigma_n(t, \xi)}{\sigma_n^*(t)} = \frac{\xi - s(t)}{s^* - s(t)} \equiv f_n(s(t), \xi), \quad \xi \in D_2(t), \tag{3.5}$$

where $f_n(s(t), \xi)$ is a linear function with respect to ξ, and varies with time since $s(t)$ and $\sigma_n^*(t)$ change during a line impact.

(b) Resultant forces and net moments

Suppose the stresses along the direction of the prism axis are homogeneous. Integrating the normal interface stress on the effective region $D_2(t)$ can express the resultant force $F_n(t)$ as a function with regard to $s(t)$ and $\sigma_n^*(t)$.

$$F_n(t) = l \int_{D_2} \sigma_n(t, \xi)\, \mathrm{d}\xi \triangleq g_1(s(t))\sigma_n^*(t), \tag{3.6}$$

where $g_1(s(t))$ is a function with respect to $s(t)$ and depends on the mode of the stress distribution. For the four kinds of modes from DS-I to DS-IV, we have

$$g_1(s(t)) = \begin{cases} \frac{1}{2}(b - s(t))l, & s(t) > 0 \text{ in DS-I} \\ \frac{1}{2}sl, & s(t) > 0 \text{ in DS-II} \\ \frac{1}{2}\frac{b - 2s(t)}{b - s(t)}bl, & s(t) < 0 \text{ in DS-III} \\ \frac{b}{2s}(2s(t) - b)l, & s(t) > 0 \text{ in DS-IV.} \end{cases} \tag{3.7}$$

The normal stress in a linear distribution also generates net moment $M_n^c(t)$ about the centre of mass C, which is given by

$$M_n^c(t) = l\int_{D_2} \sigma_n(t,\xi)\left(\xi - \frac{b}{2}\right)\mathrm{d}\xi \triangleq g_2(s(t))\sigma_n^*(t), \tag{3.8}$$

where function $g_2(s(t))$ also depends on the mode of the distribution of normal stress and takes a form as follows:

$$g_2(s(t)) = \begin{cases} \frac{1}{12}(b^2 + bs(t) - 2s^2(t))l, & s(t) > 0 \text{ in DS-I} \\ \frac{1}{12}(2s(t) - 3b)sl, & s(t) > 0 \text{ in DS-II} \\ \frac{1}{12}\frac{b^3 l}{b - s(t)}, & s(t) < 0 \text{ in DS-III} \\ -\frac{1}{12}\frac{b^3 l}{s(t)}, & s(t) > 0 \text{ in DS-IV.} \end{cases} \tag{3.9}$$

Besides the impact-agitating normal interaction, surface friction also affects the response of a line impact. Suppose Coulomb's Law can access friction property at a stress level. Then, the normal and tangential stresses at every point satisfy a relationship given by

$$\begin{cases} \dfrac{\tau(t,\xi)}{\sigma_n(t,\xi)} = -\mu \operatorname{sign}(v^\tau(t,\xi)), & \text{if } v^\tau(t,\xi) \neq 0, \\ \dfrac{|\tau(t,\xi)|}{\sigma_n(t,\xi)} \leq \mu_s, & \text{if } v^\tau(t,\xi) = 0, \end{cases} \quad \xi \in D_2(t), \tag{3.10}$$

where μ and μ_s are the slip and stick coefficient of friction, respectively, and $v^\tau(t,\xi)$ is the tangential velocity of the contacting surface at position ξ. Note that $\operatorname{sign}(v^\tau(t,\xi)) = 1$ if $v^\tau(t,\xi) > 0$, and $\operatorname{sign}(v^\tau(t,\xi)) = -1$ when $v^\tau(t,\xi) < 0$.

By assumption A1 that admits to ignore the tangential deformation in the boundary layer, together with the kinematical relationship shown in equation (2.5), the tangential velocity $v^\tau(t,\xi)$ at every point on the contact surface will take the same value at the same time. Therefore, all the points on the contact surface will either slip or stick synchronically. Obviously, the micro-slip motion, as discussed by Mindlin [27] in studying the contact problem between elastic bodies, will be excluded from our model.

Under the discussion above, we can define a generalized Coulomb's Law of using a ratio between $F_\tau(t)$ and $F_n(t)$ to govern the friction related to the prism's macroscopic motion

$$\left.\begin{aligned} F_\tau(t) &= -\mu \operatorname{sign}(v^\tau(t,\xi))F_n(t) \quad \text{if } v^\tau(t,\xi) \neq 0 \\ \text{and} \qquad |F_\tau(t)| &\leq \mu_s F_n(t) \quad \text{if } v^\tau(t,\xi) = 0. \end{aligned}\right\} \tag{3.11}$$

In a slip state of friction, $F_\tau(t)$ is linked with $F_n(t)$ by a slip coefficient μ. While in a stick state of friction, equation (3.11) provides a velocity constraint $v^\tau(t,\xi)=0$. Differentiating the condition with time gives a relationship as follows:

$$\dot{v}^\tau(t)=\ddot{x}(t)\cos\beta-\ddot{y}(t)\sin\beta+\ddot{\theta}(t)a_0\cos\alpha=0. \tag{3.12}$$

The combination of equations (3.12) and (2.3) determines a unique relationship between $F_\tau(t)$ and $F_n(t)$ as friction is in a stick state. The transition from a stick to a slip state can be distinguished by the upper bound μ_s in Coulomb's friction law. While the transition from a slip to a stick state is identified by checking whether the tangential velocity vanishes or not.

Note the centre of mass C apart from any side surface with the same distance $a_0\cos\alpha$. The net moment of $F_\tau(t)$ about mass centre C can be expressed as

$$M_\tau^c(t)=F_\tau(t)a_0\cos\alpha. \tag{3.13}$$

Since $F_n(t)$ has been expressed as a function with respect to $s(t)$ and $\sigma_n^*(t)$, both $F_\tau(t)$ and $M_\tau^c(t)$ are also functions of $s(t)$ and $\sigma_n^*(t)$ via $F_n(t)$.

(c) Impulsive differential equations

Suppose that a line impact occurs at time t_l^-. From the start of the line impact, the evolution of $\sigma_n^*(t)$ can be scaled by the normal stress impulse p^*, which is expressed as

$$p^*=\int_{t_l^-}^{t}\sigma_n^*(t)\,\mathrm{d}t \tag{3.14}$$

and is related to a differential form expressed as follows:

$$\mathrm{d}p^*=\sigma_n^*(t)\,\mathrm{d}t. \tag{3.15}$$

Here, variable p^* is continuous, though the profile of the normal-contact-stress may change from one mode to another due to the evolution of interface stress during a line impact.

Rewrite equation (2.3) into an equivalent form as follows:

$$\left.\begin{aligned} m\,\mathrm{d}\dot{x}&=\sin\beta F_n(t)\,\mathrm{d}t+\cos\beta F_\tau(t)\,\mathrm{d}t,\\ m\,\mathrm{d}\dot{y}&=\cos\beta F_n(t)\,\mathrm{d}t-\sin\beta F_\tau(t)\,\mathrm{d}t-F_L\,\mathrm{d}t\\ \text{and}\qquad J\,\mathrm{d}\dot{\theta}&=M_n^c(t)\,\mathrm{d}t+a_0\cos\alpha F_\tau\,\mathrm{d}t. \end{aligned}\right\} \tag{3.16}$$

Define $\mathrm{d}P_\tau\triangleq F_\tau(t)\,\mathrm{d}t$, $\mathrm{d}P_n\triangleq F_n\,\mathrm{d}t$. Based on the invariable configuration and the ignorable non-impulsive force as given in assumption A2, we can further simplify (3.16) by (3.6) and (3.8) into a form:

$$\left.\begin{aligned} m\,\mathrm{d}\dot{x}&=\sin\beta g_1(s(t))\,\mathrm{d}p^*+\cos\beta\,\mathrm{d}P_\tau,\\ m\,\mathrm{d}\dot{y}&=\cos\beta g_1(s(t))\,\mathrm{d}p^*-\sin\beta\,\mathrm{d}P_\tau\\ \text{and}\qquad J\,\mathrm{d}\dot{\theta}&=g_2(s(t))\,\mathrm{d}p^*+a_0\cos\alpha\,\mathrm{d}P_\tau. \end{aligned}\right\} \tag{3.17}$$

Under coulombic friction, the differential tangential impulse $\mathrm{d}P_\tau$ is related to the differential normal impulse $\mathrm{d}P_n$ in the same way as the tangential force to the normal force. The generalized coulombic friction in (3.11) can be equally rewritten as follows:

$$\left.\begin{aligned} \mathrm{d}P_\tau(t)&=-\mu\,\mathrm{sign}(v^\tau(t,\xi))\,\mathrm{d}P_n(t) && \text{if } v^\tau(t,\xi)\neq 0\\ \text{and}\qquad |\mathrm{d}P_\tau(t)|&\le\mu_s\,\mathrm{d}P_n(t) && \text{if } v^\tau(t,\xi)=0, \end{aligned}\right\} \tag{3.18}$$

which permits a unique relationship between $\mathrm{d}P_\tau(t)$ and $\mathrm{d}P_n(t)$ for the prism's motion in various tangential states. Using (3.18) and (3.6), together with (3.12), we get a relationship between $\mathrm{d}P_\tau$ and $\mathrm{d}p^*$

$$\mathrm{d}P_\tau \triangleq g_3(s(t))\,\mathrm{d}p^*, \tag{3.19}$$

where

$$g_3(s(t)) = \begin{cases} -\mu\,\mathrm{sign}(v^\tau(t,\xi))g_1(s(t)) & \text{if } v^\tau(t,\xi)\neq 0 \\ -\dfrac{ma_0\cos\alpha}{J+ma_0^2\cos^2\alpha}g_2(s(t)) & \text{if } v^\tau(t,\xi)=0. \end{cases} \tag{3.20}$$

Then, equation (3.17) becomes

$$\left.\begin{aligned} m\,\mathrm{d}\dot{x} &= (\sin\beta g_1(s(t)) + \cos\beta g_3(s(t)))\,\mathrm{d}p^*, \\ m\,\mathrm{d}\dot{y} &= (\cos\beta g_1(s(t)) - \sin\beta g_3(s(t)))\,\mathrm{d}p^* \\ \text{and}\quad J\,\mathrm{d}\dot{\theta} &= (g_2(s(t)) + a_0\cos\alpha g_3(s(t)))\,\mathrm{d}p^*. \end{aligned}\right\} \tag{3.21}$$

Since $\sigma_n^*(t)\geq 0$ in a line impact, the value of p^* will monotonically increase with time. This means that (3.21) can be thought of as a set of first-order impulsive differential equations with respect to a 'time-like' variable $\mathrm{d}p^*$.

At the initial moment t_l^- of a line impact, equation (2.1) provides the pre-impact state of the prism, including the velocity of the mass centre $\dot{x}(t_l^-)$, $\dot{y}(t_l^-)$ and the angular velocity $\dot{\theta}(t_l^-)$. These quantities initialize the impulsive differential equations (3.21).

During a line-impact phase, the value of $s(t)$ usually changes, and the position of the contact point with p^* may vary if the normal-contact-stress distribution changes from one mode to another. Furthermore, a terminal value should be specified to p^* as it is taken as an independent variable. Therefore, before (3.21) is adopted to obtain the post-impact outputs, we should determine how the normal stress evolves on the contact interface and have to find the condition by which a line impact is terminated.

(d) Potential energy density and stress–energy relationship

In order to reflect the evolution of the normal stress during a line impact, let us establish a relationship between the normal interface stress and the potential energy reserving in the boundary layer. This can be implemented according to the stress–strain relationship specific to the boundary layer.

Let us denote by $\Pi_n(t,\xi)$ a potential-energy-density function to consider the potential energy reserving in per unit thickness of the elastic boundary layer. Its increment $\mathrm{d}\Pi_n(t,\xi)$ at a given contact point can be calculated by stress $\bar{\sigma}_n(t,\xi)$ timing an infinitesimal normal strain $\mathrm{d}\varepsilon_n(t,\xi)$ in the internal of the boundary layer. Noting that $\bar{\sigma}_n(t,\xi)$ is opposite to the normal interface stress $\sigma_n(t,\xi)$. The increment $\mathrm{d}\Pi_n(t,\xi)$ is given by

$$\mathrm{d}\Pi_n(t,\xi) = -\sigma_n(t,\xi)\,\mathrm{d}\varepsilon_n(t,\xi) = -\mathrm{d}p(t,\xi)\dot{\varepsilon}_n(t,\xi), \quad \xi\in D_2(t), \tag{3.22}$$

where $\mathrm{d}p(t,\xi)$ and $\dot{\varepsilon}_n(t,\xi)$ are, respectively, the infinitesimal impulse of the normal interface stress and the strain rate at the same contact point.

Since both the prism and the ramp are considered as rigid bodies, and the ramp is fixed without any motion, the strain rate can be expressed as $\dot{\varepsilon}_n(t,\xi) = v^n(t,\xi)/\Delta$, and $v^n(t,\xi)$ is just the normal velocity of the point fixed on boundary AB of the rigid prism. At the start of a line impact, we have $\Pi_n(t_l^-,\xi)=0$ and $p(t_l^-,\xi)=0$. So, function $\Pi_n(t,\xi)$ is expressed as follows:

$$\Pi_n(t,\xi) = -\frac{1}{\Delta}\int_0^{p(t,\xi)} v^n(t,\xi)\,\mathrm{d}p(t,\xi) \equiv \frac{1}{\Delta}\bar{\Pi}_n(t,\xi), \quad \xi\in D_2(t), \tag{3.23}$$

where $\bar{\Pi}_n(t,\xi) = \int_0^{p(t,\xi)} v^n(t,\xi)\,\mathrm{d}p(t,\xi)$.

When $v^n(t,\xi)<0$, corresponding to a compressional phase at the point, $\Pi_n(t,\xi)$ increases due to the motion of the prism. As the contact point is in an expansion phase ($v^n(t,\xi)>0$), $\Pi_n(t,\xi)$

decreases. For a fully elastic contact, its reduction will be fully transferred into the kinetic energy confined in the motion of the prism.

Note that $\Pi_n(t,\xi)$ couples with the normal stress that should satisfy the stress–strain relationship specified to the elastic boundary layer. According to the stress–strain relationship in equation (3.2), together with the substitution of $\sigma_n(t,\xi)$ for $\bar{\sigma}_n(t,\xi)$, its differential with regard to time t can be given by

$$\frac{\partial \sigma_n(t,\xi)}{\partial t} = -E^* \frac{\partial \varepsilon_n(t,\xi)}{\partial t} = \begin{cases} -\dfrac{E^*}{\Delta} v^n(t,\xi), & \xi \in D_2(t) \\ 0, & \xi \in D_1(t), \end{cases} \tag{3.24}$$

where $v^n(t,\xi) = \partial\delta(t,\xi)/\partial t$.

Timing (3.24) with $\sigma_n(t,\xi)$ on both sides of it and noticing that $\mathrm{d}p(t,\xi) = \sigma_n(t,\xi)$, we have

$$\sigma_n(t,\xi)\,\mathrm{d}\sigma_n(t,\xi) = -\frac{E^*}{\Delta} v^n(t,\xi)\,\mathrm{d}p(t,\xi), \quad \xi \in D_2(t). \tag{3.25}$$

Integrating (3.25) by an initial condition $\sigma_n(t_l^-,\xi) = 0$, together with (3.23), leads to

$$\frac{1}{2}\sigma_n^2(t,\xi) = -\frac{E^*}{\Delta}\int_0^{p(t,\xi)} v^n(t,\xi)\,\mathrm{d}p(t,\xi) = \frac{E^*}{\Delta}\bar{\Pi}_n(t,\xi), \quad \xi \in D_2(t). \tag{3.26}$$

So we have

$$\sigma_n(t,\xi) = \frac{\mathrm{d}p(t,\xi)}{\mathrm{d}t} = \sqrt{\frac{2E^*}{\Delta}\bar{\Pi}_n(t,\xi)}, \quad \xi \in D_2(t). \tag{3.27}$$

Equation (3.27) establishes a relationship between normal interface stress $\sigma_n(t,\xi)$ and potential energy density $\bar{\Pi}_n(t,\xi)$.

(e) Evolution of the normal interface stress

Once the relationship between normal interface stress and potential energy density is established, the evolution of the normal interface stress can be quantified by $\bar{\Pi}_n(t,\xi)$ whose value will be timely updated through the solutions of the dynamics of a line impact.

Note the feature of the normal interface stress with a linear distribution. Its evolution is basically determined by the values of s^* and $s(t)$. Once both the values are determined, the instantaneous profile of the normal interface stress can be obtained, then the dynamics of a line impact governed by (3.21) is advanced via impulse p^* increasing monotonically like a time variable.

At the start of a line impact, we have $v^n(t_l^-,0) = 0$ and the magnitude of $v^n(t_l^-,b)$ is the maximum. So, the normal-contact-stress distribution in the line impact will take a shape in mode DS-I with an effective region $D_2(t_1^-) = [0,b]$. At this time, the point with the value of p^* is at B, and we have $s(t_l^-) = 0$, $s^*(t_l^-) = b$, $p^*(t_l^-) = 0$. Consequently, the values of $g_i(0)$, $(i = 1,2,3)$, are known.

By allowing p^* with an increment $\mathrm{d}p^*$, we can calculate by (3.21) the variations of the velocities in the prism's motion induced by the increment $\mathrm{d}p^*$. At the same time, the velocity distribution on the contact surface can also be calculated by the kinematics specific to the rigid motion of the prism.

The potential-energy density complies with the velocity distribution on the contact surface. Therefore, as $v^n(t,\xi)$ varies, the instantaneous value of $\bar{\Pi}_n(t,\xi)$ at any point also changes and can be obtained by (3.23). Owing to the linear distribution, at any given instant we only need two values of $\bar{\Pi}_n(t,\xi)$ for determining the distribution profile of the normal stress.

Let us arbitrarily select two distinct contact points, $\xi_1, \xi_2 \in D_2$. The values of $\bar{\Pi}_n(\xi_1,t)$ and $\bar{\Pi}_n(\xi_2,t)$ can then be calculated by (3.23) according to the outputs of (3.21) over the increment $\mathrm{d}p^*$. By the combination of (3.27) and (3.5), we have

$$\sqrt{\frac{\bar{\Pi}_n(t,\xi_1)}{\bar{\Pi}_n(t,\xi_2)}} = \frac{\xi_1 - s(t)}{\xi_2 - s(t)}. \tag{3.28}$$

Equation (3.28) provides a new value of $s(t)$ in association with the variation of the potential energy on the elastic boundary layer, and $\bar{\Pi}_n(t, s(t)) = 0$. Meanwhile, we can directly compare the values of $\bar{\Pi}_n(t, 0)$ and $\bar{\Pi}_n(t, b)$, corresponding to the potential energy density at A and B, respectively. If $\bar{\Pi}_n(t, b) > \bar{\Pi}_n(t, 0)$, the stress at point B is maximum, such that it is related to the independent variable p^*, and $s^* = b$. Otherwise, the maximal normal stress appears at A, so the independent variable p^* should be designated to the stress impulse at point A, and $s^* = 0$. Note that any negative value cannot be permitted by $\bar{\Pi}_n(t, \xi)$. Its occurrence means that part of the interface has lost contact stress.

Based on the values of $s(t)$ and s^*, we can distinguish the mode of the normal-contact-stress distribution at current time, then update the values of $g_i(s(t))$, $(i = 1, 2, 3)$. By prescribing a new increment to p^*, and repeating the process shown above, the dynamics of a line impact (3.21) can then be advanced along with p^* until a condition to terminate the line impact is met.

Although the line-impact model presented in this paper is based on Winkler's elastic base to model material behaviours activated by impacts, the concrete values of the thickness of the boundary layer and the elastic modulus of materials are not required. This allows our model to take advantages over the techniques of using a spring-dashpot model, which require the above values for the calculations of small deformation.

(f) Energy dissipation

When the boundary layer is elastic, it means that no dissipation is taken into account in modelling. However, impact always triggers complex material behaviours that inevitably dissipate certain mechanical energy.

To scale the energy dissipation of a line impact in a disc–ball system [15], we discretize a line impact into a series of impacts at lumped points in which a coefficient of restitution is used for considering energy dissipation. Although this method is validated by the good agreements between our numerical and experimental results, the line impact specific to the prism's motion allows us to scale the energy dissipation in a simpler way.

Under assumption A3, the intensity of a line impact is not big, so the prism cannot enter into a free motion after a line impact. According to our experimental observation, this assumption is available for the prism with a large edge number N rolling on a ramp in a small inclined angle. This scenario can be described as a non-detachment condition that allows one of the prism's edges to keep contacting the ramp after a line impact. Mathematically, a line impact finishes at the instant when the following kinematic relationship is satisfied:

$$v^n(t_l^+, b) = 0, \quad \text{or} \quad v^n(t_l^+, 0) = 0; \quad \text{and} \quad v^n(t_l^+, \xi) \geq 0 \quad \text{for all } \xi \in D. \tag{3.29}$$

Once the above condition is met, the solutions by (3.21) at current time are thought of the outputs of a line impact. Its outputs are then adopted to initialize the subsequent motion of the prism with a fixed-axis rotation.

At the instant of the condition satisfied, the effective region D_2 is usually not null. This means that certain potential energy will be discarded at the end of a line impact. In this sense, the condition in (3.29) plays a role of scaling the dissipation of the energy occurring in a line impact.

(g) The prism's rolling motion independent of material

As a prism is in a pure rotation around an edge, its governing equation of (2.1) obviously shows that the prism's dynamics is independent of mass m and the coefficient of friction. Therefore, the pure rotation will be independent of materials if the stick state in friction can be kept in the dynamics. In addition, we can prove that the output of a line impact is also independent of the prism's material.

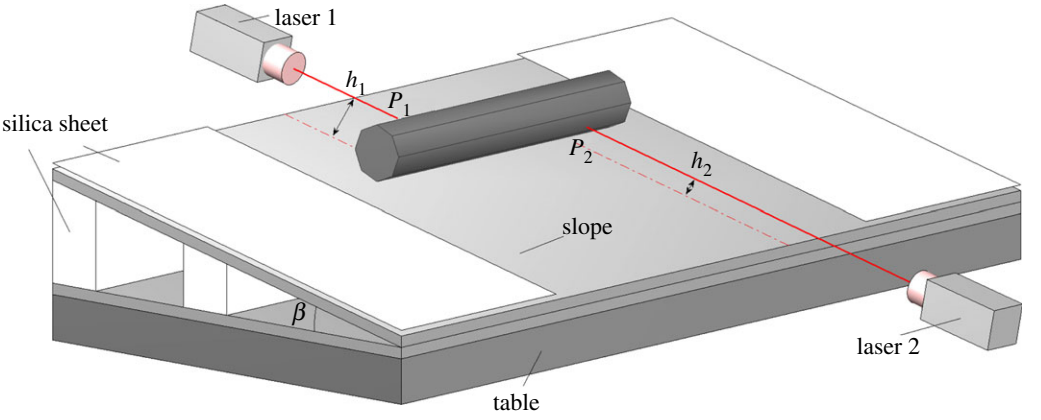

Figure 4. Schematic of the experiment system for a prism rolling on a ramp. (Online version in colour.)

Let us replace the independent normal stress impulse p^* by $\bar{p}^* = p^*/m$, which scales p^* by the prism's mass m. After that, the impulsive differential equation in (3.21) is equally rewritten as

$$\left.\begin{aligned} \mathrm{d}\dot{x} &= (\sin\beta g_1(s(t)) + \cos\beta g_3(s(t)))\,\mathrm{d}\bar{p}^*, \\ \mathrm{d}\dot{y} &= (\cos\beta g_1(s(t)) - \sin\beta g_3(s(t)))\,\mathrm{d}\bar{p}^* \\ \text{and} \quad \left(\frac{J}{m}\right)\mathrm{d}\dot{\theta} &= (g_2(s(t)) + a_0\cos\alpha g_3(s(t)))\,\mathrm{d}\bar{p}^*. \end{aligned}\right\} \tag{3.30}$$

Note that ratio J/m is irrelevant to m. As the stick state remains unchanged, the value of $s(t)$, determined by the outputs of (3.30) at each step of p^*, is independent of m, so does for functions $g_i(s(t))$. Therefore, the evolution of (3.30) is independent of m. In addition, the terminal condition (3.29) for a line impact is of geometric consistence to be unaffected by mass m. When this condition is incorporated into the line impact model, the outputs of a line impact will be material-independent. The combination of the material-independent properties for the dynamics in line impacts and in fixed-axis rotation makes the prism's rolling motion independent of the material. This property will be validated via the following numerical and experimental investigations.

4. Experimental set-up, measurement method and physical parameters

Figure 4 shows a schematic of the experimental system for a prism rolling on a ramp. Experiments are committed on an experiment table that provides a quite horizontal standard. A glass plate, with thickness 15 mm and a uniformly rough surface of 650 × 300 mm, is inclined to form a ramp in a small angle β to the horizontal plane. An alternative steel plate with the same shape as the glass plate is also used for checking the rolling motion on different rough surfaces.

Six prisms with different edge number N are fabricated from identical steel rods with the same radius $a_0 = 15$ mm and the same length $l = 50$ mm. In order to examine the effects of material on the prism's rolling motion, we also experimentally test two aluminium prisms with shapes the same as the steel prisms with edge number $N = 22$ and 30. To make sure the flatness of the side surfaces, all the prisms are precisely machined via a numerical control machine and are galvanized to make their side surfaces reflect light effectively.

In experiments, we first place the prism in contact with the ramp by an edge, tilt it with an initial angle λ_0, then release it to trigger a rolling motion. It should be noted that the release configuration of the prism is limited to a value of $\lambda_0 < \alpha + \beta$ for the prism rolling forward. Otherwise, the prism will fall down backwards due to gravity. Also, the inclined angle β must be set at a small value in order to make the prism keep rolling without detachment.

Owing to impacts, high-frequency vibration will be excited along the prism's rolling motion. The agitated vibration may change the friction on the contact surface, which in turn influences

the prism's motion. For achieving a stable rolling motion, it is important to damp the impact-agitating vibration by taking some measures. In our experiments, silica sheets are put under the slope, and over the inclined surface outside the rolling route of the prism.

Two laser-Doppler vibrometers (Polytec-OFV-3001-353) are adopted to measure the prism's motion. Data acquisition is performed via an analogue-to-digital card (PMD-1608FS) with a sample rate 10 kHz. A method of mirror reflection is used to guarantee the directions of the two laser beams parallel to the ramp. Namely, the laser beam can be reflected back along the same route as it shoots to a mirror vertical to the ramp. Owing to the creep effects in silica materials, the parallelism of the two laser beams has to be carefully adjusted for each test in order to obtain reliable experimental data. We also use a high-speed (CCD) camera to capture the prism's motion.

The two parallel laser beams intersect the corresponding surface of the rolling prism at two measured points, designated by p_1 and p_2, and a distance h_1 and h_2 apart on the ramp, respectively. Suppose $v_{p_1}(t)$ and $v_{p_2}(t)$ the instantaneous components of the velocities of the two measured points along the ramp direction. The rotary velocity of the rolling prism can be given by

$$\dot{\theta}(t) = \frac{v_{p_1}(t) - v_{p_2}(t)}{h_1 - h_2}. \tag{4.1}$$

Integration of $\dot{\theta}(t)$ can give the angle $\theta(t)$ passed by a rolling prism. The times of line impacts occurring in a prism with N edge number performing a rotary angle $\theta(t)$ can be calculated by

$$L_p(t) = \frac{N\theta(t)}{2\pi}. \tag{4.2}$$

Note that the two gauged points p_1 and p_2 are not fixed on the prism, but comply with the positions instantaneously intersected by two laser beams. According to the outputs of the prism's dynamics in simulations, the corresponding values of $v_{p_1}(t)$ and $v_{p_2}(t)$ can be calculated via a relationship expressed as follows:

$$v_{p_i}(t) = \dot{x}(t)\cos\beta - \dot{y}(t)\sin\beta - \dot{\theta}(t)(h_i - (y(t)\cos\beta + x(t)\sin\beta)), \tag{4.3}$$

where $i = 1, 2$ for points p_1 and p_2, $(x(t), y(t))$ and $(\dot{x}(t), \dot{y}(t))$ are the position and velocity of the prism's centre of mass, respectively.

5. Numerical and experimental results

In this section, we will experimentally and numerically investigate the rolling motions of prisms under different conditions, including the changes in materials and friction as well as prism geometries. Although the slip state in friction can access our model, we focus on a specific scenario in which neither slip nor detachment occurs in the whole process of the prism's rolling. This special case, denoted as a *pure rotation*, allows the model of a line impact to be examined in a clear physical picture with the manifestation of energy dissipation coming from the factor of impact-agitating vibration. In addition, theoretical analysis indicates that the pure rotation is independent of materials. This property benefits solidifying of our model through observing prisms in different materials rolling on different contact surfaces.

(a) Validation for the pure rotation in prism's motion

Capturing the prism's motion by a high-speed camera can provide a vivid observation to examine whether slip or detachment occurs. The electronic supplementary material video (see footnote 1) shows a steel prism with 24 edges rolling on a glass ramp. It clearly reveals that the prism rotates firstly around an edge, then changes its rolling axis via a line impact to another edge, and repeats this process continually to form a pure rotation.

This phenomenon can be quantified by our experimental data. In our experiments, the two laser sensors shoot two beams apart from the glass ramp with a distance $h_1 = 19.9$ mm and $h_2 = 11.6$ mm, respectively. The beam with a direction opposite to the prism's motion

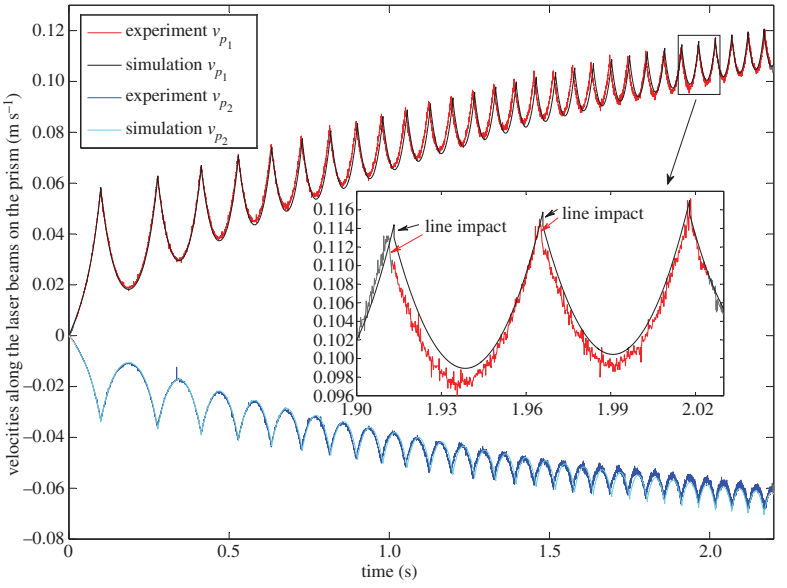

Figure 5. A steel prism with $N = 22$ rolling on a glass ramp at an inclined angle $\beta = 0.4079^\circ$. Comparison between numerical and experimental results for the velocities of the gauged points p_1 and p_2 with distances $h_1 = 19.9$ mm and $h_2 = 11.2$ mm apart on the ramp, respectively. Inset details the dynamics adjacent to a line impact. (Online version in colour.)

measures the velocity $v_{p_1}(t)$ with positive values, while the other one along the prism's motion measures velocity $v_{p_2}(t)$ with negative values.

Figure 5 shows the curves of $v_{p_1}(t)$ and $v_{p_2}(t)$ versus time for a steel prism with $N = 22$. Just after releasing it, the prism rotates about an edge on the ramp and is accelerated by gravity to make the magnitudes in $v_{p_1}(t)$ and $v_{p_2}(t)$ increase monotonically. When $\lambda = 0$, a line impact occurs. After that, the prism retrieves its rotation around a subsequent edge, then keeps rolling on the ramp.

The cuspids in the curves correspond to the instant of line impacts, which not only change the magnitude of the rotary velocity of the prism, but also alter its rolling axis. The inset in figure 5 shows a detailed inspection of the values of $v_{p_1}(t)$ related to the prism's motion passing through three times of line impacts. Clearly, only one sharp step exists at each individual cuspid in the curves. This means that a line impact reduces the magnitude of the rotary velocity, but cannot allow the prism to detach away from the ramp (the occurrence of other impacts will generate multiple steps in the curves). Therefore, the prism after the impact begins to rotate about the subsequent edge. Note that the concave shape in the curves is attributed to the different roles of gravity that first resists then accelerates the rotation along the prism changing its configuration. The rotation decelerates during the time interval when the prism's configuration changes from $\lambda = 2\alpha$ to $\lambda = \alpha + \beta$, then accelerates until another line impact occurs.

Referring to the material manual, we estimate the glass–steel contact surface with a stick coefficient $\mu_s = 0.12$. This value is applied to our simulations to check the friction state in line impacts and in the rotation of the prism about an edge. Our numerical simulations indicate that the prism follows a pure rotation, namely no slip and no detachment occur on the contact surface. By setting the prism with an initial configuration $\lambda_0 = 5.3220^\circ$, good agreements are achieved in the comparisons between our numerical and experimental results.

(b) Energy dissipation in a pure rotation

As a prism rotates about a fixed axis without slippage, no energy is dissipated. Therefore, the energy dissipated in the motion of a prism only comes from the events of line impacts. When slip friction and material plasticity are excluded from the dynamics of a line impact, the unique

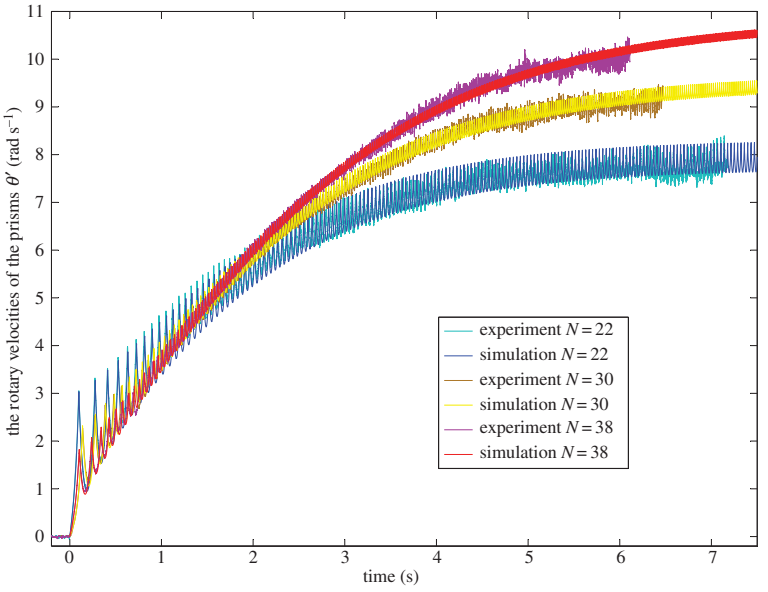

Figure 6. Comparison between numerical and experimental results for rotary velocities of prisms with $N = 22, 30, 38$ rolling on a glass ramp ($\beta = 0.4079^\circ$). Numerical simulations are performed by setting $\lambda_0 = 7.2^\circ,\ 5.3220^\circ,\ 4.5^\circ$, respectively. (Online version in colour.)

factor responsible for dissipation is just the impact-agitating vibration that is scaled in our model via a kinematical condition given by equation (3.29) to terminate the process of a line impact. This condition makes the rotary axes of a prism change from one edge to another, and manifests dissipation of energy by the sharp decrease in the rotary velocity at the instant of a line impact.

Note that certain gravitational potential energy will be transferred into the rotation of a prism. If the energy dissipated in an individual line impact is less than the pumped energy related to the prism rolling a central angle $2\pi/N$, the average rotary velocity will continuously increase. Once the two parts of energy can be balanced, the rotary velocity will vary periodically with a period the same as the time interval of two adjacent impacts, and the prism moves along the ramp like an ideal cylinder performing a pure rotation with a uniform rotary velocity.

Figure 6 plots the rotary velocities for three steel prisms with $N = 22, 30, 38$ rolling on a glass ramp. In their initial stages, the motion of these prims follows an approximately uniform accelerative motion. With the increase of rolling velocity, more energy will be dissipated in each individual line impact. This will reduce the rolling acceleration to make the curves of the rotary velocity in convex shapes. When balance is reached between the pumped energy by gravity and the dissipated energy by line impacts, each curve of the rotary velocity will reach a distinct platform accompanying local fluctuations. The curves in figure 6 clearly reveal this tendency, though no perfect platforms appear due to the limitation of the ramp's length. Figure 6 also shows that our numerical results can precisely agree with the experimental findings.

(c) The prism's motion independent of material

According to the model proposed in this paper, the prism's motion in a pure rotation mode is independent of the material. We use a high-speed camera to record the motions of two prisms with the same shape ($N = 30$) but one made from steel and the other from aluminium. When they are released in the same configuration on the glass slope, the electronic supplementary material, video (see footnote 1), clearly shows that the two prisms roll synchronically on the ramp in the same fashion.

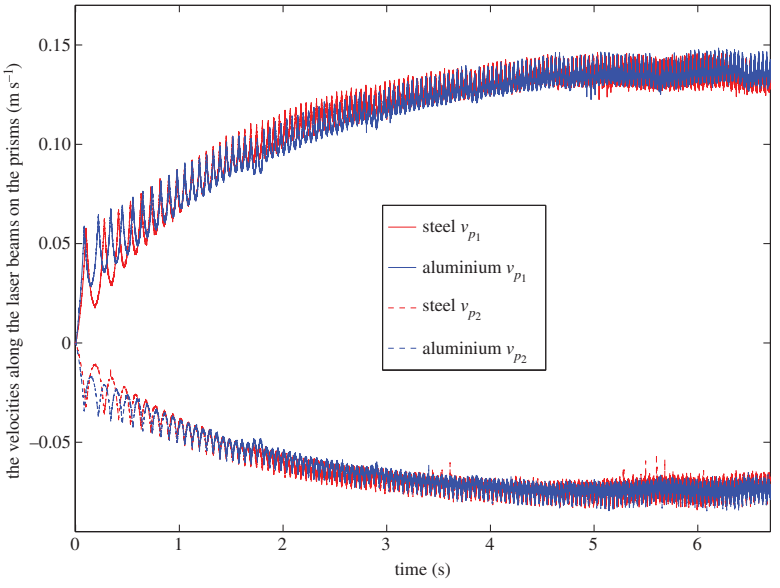

Figure 7. Velocities at the gauged points p_1 and p_2 with distances $h_1 = 22.3$ mm and $h_2 = 11.9$ mm for a steel prism and an aluminium prism with the same edge number $N = 24$, separately released on the same glass ramp with an inclined angle $\beta = 0.3702^\circ$. (Online version in colour.)

This property is further confirmed by comparing the experimental results for the prisms with $N = 24$ in steel and aluminium materials, respectively. We plot the two sets of experimental results in figure 7. Although the two experiments are performed separately to generate obvious deviation in the initial stages of their motions, the two prisms will quickly converge to a synchronously rolling motion. This also means that the perturbation in its initial configuration has little effect on the long-term behaviour of a prism's motion.

(d) Prisms with different edge number in rolling motion

By using prisms with different edge number, we numerically and experimentally investigate the effect of N on the rolling motion of prisms. The investigation concerns six steel prisms with identical radius $a_0 = 15$ mm and the same length $l = 50$ mm, while the edge number varies with $N = 22, 24, 30, 32, 36, 38$. All the experiments are performed on the same glass ramp with the same inclined angle $\beta = 0.3792^\circ$. Simulations are implemented by specifying the initial configuration $\lambda_0 = 7.2^\circ$, 5.25°, 5.3220°, 4.8937°, 5.06°, 4.5°, to the corresponding prism along increasing N.

In order to explicitly expose the difference of the rolling motion in the six prisms, we plot line-impact times $L_p(t)$ versus time in figure 8. Aside from the good agreements between our numerical and experimental results, these curves clearly show that the prism runs faster as N increases. This implies that the line impacts in the prism dissipate less energy as the edge number N increases.

(e) Prisms rolling on different contact interfaces

In order to check the rolling motion of the prism on different contact surfaces, we re-examine the rolling motion of the six steel prisms by setting them on a steel ramp. Experimental measurements are performed by setting the heights of the two laser beams apart from the steel ramp at distances $h_1 = 22.3$ mm and $h_2 = 11.9$ mm.

In comparison with the glass–steel surface, the steel–steel contact surface reduces friction with a small value for the stick coefficient ($\mu_s = 0.08$). Under the friction property, details of simulations and experiments indicate that no slip and no detachment can occur in the motion of these prisms.

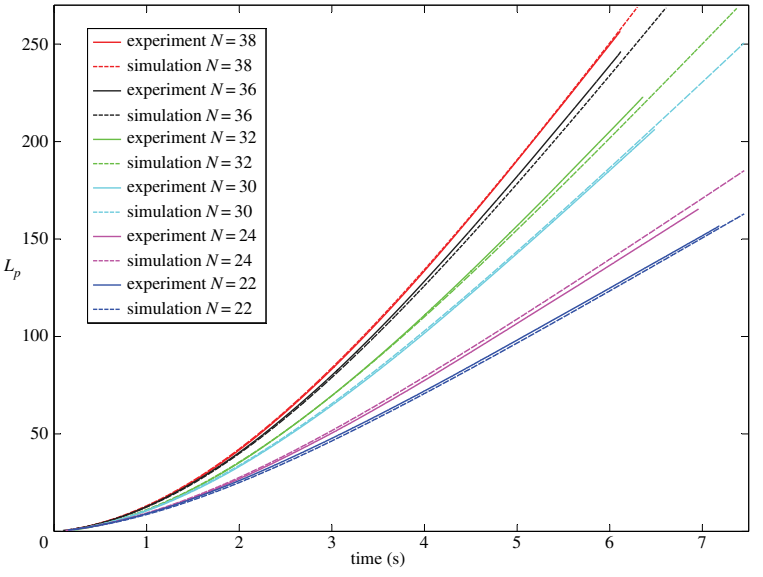

Figure 8. Line-impact times $L_p(t)$ in six steel prisms with $N = 22, 24, 30, 32, 36, 38$ rolling on a glass ramp with an inclined angle $\beta = 0.3702^\circ$. Numerical simulations are performed by setting the prisms at their corresponding initial configurations $\lambda_0 = 7.2^\circ,\ 5.25^\circ,\ 5.3220^\circ,\ 4.8937^\circ,\ 5.06^\circ,\ 4.5^\circ$. The maximum relative errors between the numerical and experimental results are 0.39%, 2.19%, 1.79%, 0.69%, 2.54% and 0.75% from $N = 22$ to $N = 38$. (Online version in colour.)

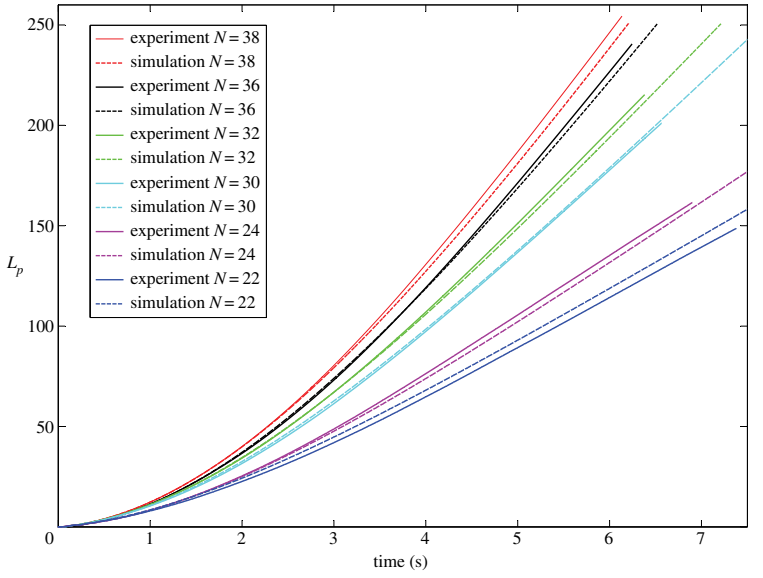

Figure 9. Line-impact times $L_p(t)$ in six steel prisms with $N = 22, 24, 30, 32, 36, 38$ rolling on a steel ramp with an inclined angle $\beta = 0.3792^\circ$. Numerical simulations are performed and the maximum relative errors between the numerical and experimental results are 4.42%, 1.73%, 0.837%, 1.71%, 1.12% and 3.08% from $N = 22$ to $N = 38$. (Online version in colour.)

Figure 9 presents our numerical and experimental results for the values of L_p in the six steel prisms. In comparison with the experiments on a steel–glass contact surface, the change of material on the contact surface slightly enlarge the discrepancies between our numerical and experimental data. The discrepancies essentially come from small-scaled behaviours in the impact-agitating vibration. According to our experimental observations, vibration is more easily agitated on the steel–steel surface than on the steel–glass surface. Although certain measures

were taken to alleviate the vibration, its effects on the friction of the contact surface cannot be completely annihilated.

6. Conclusion and discussion

In this paper, we have theoretically and experimentally studied a planar prism rolling on a fixed ramp inclined at a small angle. In order to deal with the problem of line impacts involved in the prism's motion, we propose a line-impact model that can properly reflect the dissipation and dispersion of energy occurring on the contact surface. Validation of the theoretical development is supported by the good agreements between our numerical and experimental results related to motions of many prisms made in distinct shapes and in different materials.

Essentially, a line impact agitates complex material behaviours with different size scales during an extremely small time interval. By scaling these behaviours into an elastic boundary layer with a linear stress–strain relationship and Coulomb's friction, our theory clearly indicates that a line impact results in complex evolution of stress on the contact surface, which cannot be neglected in modelling. In addition, although the impact-agitating vibration only dissipates a small amount of energy in each individual impact, its accumulative effects will be manifested in the long-term behaviours of the prism's motion. Without resorting to the concrete physical mechanism, we discover that a non-detachment condition can be used to quantify the energy dissipation of a line impact.

Through systematic experiments with results agreeing with numerical simulations, we have also discovered some intriguing phenomena. If neither slip nor detachment occurs in prisms with the same edge number N, its rolling velocity is nearly unaffected by the prism's material and the friction of the contact surface. If the length of ramp is large enough, the rotary velocity will gradually converge to a constant value. Nevertheless, the value will be distinct for prisms with different edge number N. The prism will roll faster as N increases.

Imagine that an ideal circular section can be approximately equivalent to a polygon with a large enough edge number N. Approximately, the line impacts in the rolling motion of a prism can be thought of discretizing the rolling process of an elastic cylinder, while augmenting the effects of the energy dissipation by line impacts. Basically, an elastic body in contact may agitate more complex material behaviours with different scales in size and time [28–30]. Coupling of these scales will be more complex than that in the prism's pure rotation. Nevertheless, the similarity between them may allow us to expect some conclusions of this paper to apply to discovering the physical mechanism of rolling friction in an elastic cylinder.

Funding statement. This work was supported by the Natural Science Foundation of China (11172019, 11132001) and 'Fanzhou' Youth Research Foundation (20110501).

References

1. Luan B, Robbins, MO. 2005 The breakdown of continuum models for mechanical contacts. *Nature* **435**, 929–932. (doi:10.1038/nature03700)
2. Di Toro G, Han R, Hirose T, De Paola N, Nielsen S, Mizoguchi K, Ferri F, Cocco M, Shimamoto T. 2011 Fault lubrication during earthquakes. *Nature* **471**, 494–498. (doi:10.1038/nature09838)
3. Liu C, Zhao Z, Brogliato B. 2008 Frictionless multiple impacts in multibody systems. I. Theoretical framework. *Proc. R. Soc. A* **464**, 3193–3211. (doi:10.1098/rspa.2008.0078)
4. Stronge WJ. 2000 *Impact mechanics*. New York, NY: Cambridge University Press.
5. Brogliato B. 1999 *Nonsmooth mechanics: models, dynamics, and control*. London, UK: Springer.
6. Pfeiffer F, Glocker C. 1996 *Multibody dynamics with unilateral contacts*. New York, NY: Wiley.
7. Keller JB. 1986 Impact with friction. *ASME. J. Appl. Mech.* **53**, 1–4. (doi:10.1115/1.3171712)
8. Zhao Z, Liu C, Chen B. 2006 The numerical method for three dimensional impact with friction of multi-rigid-body system. *Sci. China Series G-Phys. Astron.* **49**, 102–118. (doi:10.1007/s11433-005-0065-0)

9. Saitoh K, Bodrova A, Hayakawa H, Brilliantov NV. 2010 Negative normal restitution coefficient found in simulation of nanocluster collisions. *Phys. Rev. Lett.* **105**, 238001. (doi:10.1103/PhysRevLett.105.238001)
10. Wang J, Liu C, Zhao Z. In press. Nonsmooth dynamics of a 3D rigid body on a vibrating plate. *Multibody Syst. Dyn.* (doi:10.1007/s11044-013-9385-4)
11. Crassous J, Beladjine D, Valance A. 2007 Impact of a projectile on a granular medium described by a collision model. *Phys. Rev. Lett.* **99**, 248001. (doi:10.1103/PhysRevLett.99.248001)
12. Boechler N, Theocharis G, Job S, Kevrekidis PG, Porter MA, Daraio C. 2010 Discrete breathers in one-dimensional diatomic granular crystals. *Phys. Rev. Lett.* **104**, 244302. (doi:10.1103/PhysRevLett.104.244302)
13. Daraio C, Nesterenko VF, Herbold EB, Jin S. 2006 Energy trapping and shock disintegration in a composite granular medium. *Phys. Rev. Lett.* **96**, 058002. (doi:10.1103/PhysRevLett.96.058002)
14. Liu C, Zhao Z, Brogliato B. 2009 Frictionless multiple impacts in multibody systems. II. Numerical algorithm and simulation results. *Proc. R. Soc. A* **465**, 1–23. (doi:10.1098/rspa.2008.0079)
15. Liu C, Zhang H, Zhao Z, Brogliato B. 2013 Impact-contact dynamics in a disc-ball system. *Proc. R. Soc. A* **469**, 20120741. (doi:10.1098/rspa.2012.0741)
16. Zhang H, Liu C, Zhao Z, Brogliato B. 2013 Energy evolution in complex impacts with friction. *Sci. China-Phys. Mech. Astron.* **56**, 875–881. (doi:10.1007/s11433-013-5061-1)
17. Zhao Z, Liu C, Brogliato B. 2008 Energy dissipation and dispersion effects in granular media. *Phys. Rev. E* **78**, 031307. (doi:10.1103/PhysRevE.78.031307)
18. Zhen Z, Liu C, Brogliato B. 2009 Planar dynamics of a rigid body system with frictional impacts. II. Qualitative analysis and numerical simulations. *Proc. R. Soc. A* **465**, 2267–2292. (doi:10.1098/rspa.2008.0520)
19. Abeyaratne R. 1989 The motion of a prism rolling down an inclined plane. *Int J. Mech. Eng. Educ.* **17**, 53–61.
20. McDonald KT. 2008 Hexagonal pencil rolling on an inclined plane. *Regul. Chaotic Dyn.* **13**, 332–343. (doi:10.1134/S1560354708040072)
21. Rezaeezadeh A. 2009 Motion of a hexagonal pencil on an inclined plane. *Am. J. Phys.* **77**, 401–406. (doi:10.1119/1.3098257)
22. Ruina A, Bertramb JEA, Srinivasan M. 2005 A collisional model of the energetic cost of support work qualitatively explains leg sequencing in walking and galloping, pseudo-elastic leg behavior in running and the walk-to-run transition. *J. Theoret. Biol.* **237**, 170–192. (doi:10.1016/j.jtbi.2005.04.004)
23. Jonson KL. 1985 *Contact mechanics*. Cambridge, UK: Cambridge University Press.
24. Eldredge KR, Tabor D. 1955 The mechanism of rolling friction. I. The plastic range. *Proc. R. Soc. Lond. A* **229**, 181–198. (doi:10.1098/rspa.1955.0081)
25. Dankowicz H. 1999 On the modeling of dynamics friction phenomena. *Z. Angew. Math. Mech.* **79**, 399–409. (doi:10.1002/(SICI)1521-4001(199906)79:6<399::AID-ZAMM399>3.0.CO;2-K)
26. Eriten M, Polycarpou A, Bergman LA. 2011 Physics-based modelling for fretting behaviour of nominally flat rough surface. *Int. J. Solids Struct.* **48**, 1436–1450. (doi:10.1016/j.ijsolstr.2011.01.028)
27. Mindlin RD, Deresiewicz H. 1953 Elastic spheres in contact under varying oblique forces. *Trans. ASME Series E, J. Appl. Mech.* **20**, 221–227.
28. Persson BNJ. 2010 Rooling friction for hard cylinder and sphere on viscoelastic solid. *Eur. Phys. J. E* **33**, 327–333. (doi:10.1140/epje/i2010-10678-y)
29. Greenwood JA, Minshall H, Tabor D. 1961 Hysteresis losses in rolling and sliding friction. *Proc. R. Soc. Lond. A* **259**, 480–507. (doi:10.1098/rspa.1961.0004)
30. Brilliantov NV, Pöschel T. 1998 Rolling friction of a viscous sphere on a hard plane. *Europhys. Lett* **42**, 511–516. (doi:10.1209/epl/i1998-00281-7)